

Multipartite Entanglement in Rabi-Driven Superconducting Qubits

Marie Lu,^{1,*} Jean-Loup Ville,¹ Joachim Cohen,² Alexandru Petrescu^{1,2}, Sydney Schreppler,¹ Larry Chen¹, Christian Jünger,³ Chiara Pelletti⁴, Alexei Marchenkov,⁴ Archan Banerjee,¹ William P. Livingston¹, John Mark Kreikebaum,³ David I. Santiago,³ Alexandre Blais,^{2,5} and Irfan Siddiqi^{1,3}


¹Department of Physics, University of California, Berkeley, California 94720, USA

²Institut Quantique and Département de Physique, Université de Sherbrooke, Sherbrooke, Québec J1K 2R1, Canada

³Applied Mathematics and Computational Research Division, Lawrence Berkeley National Laboratory, University of California, Berkeley, California 94720, USA

⁴Bleximo Corporation, 701 Heinz Avenue, Berkeley, California 94710, USA

⁵Canadian Institute for Advanced Research, Toronto, Ontario M5G1M1, Canada

 (Received 17 July 2022; accepted 24 October 2022; published 23 November 2022; corrected 20 December 2022)

The exploration of highly connected networks of qubits is invaluable for implementing various quantum algorithms and simulations, as it allows for entangling qubits with reduced circuit depth. Here, we demonstrate a multiqubit sideband tone-assisted Rabi-driven gate. Our scheme is inspired by the ion-qubit Mølmer-Sørensen gate and is mediated by a shared photonic mode and Rabi-driven superconducting qubits, which relaxes restrictions on qubit frequencies during fabrication and supports scalability. We achieve a two-qubit gate with a maximum state fidelity of 95% in 310 ns, a three-qubit gate with a state fidelity of 90.5% in 217 ns, and a four-qubit gate with a state fidelity of 66% in 200 ns. Furthermore, we develop a model of the gate that shows that the four-qubit gate is limited by shared resonator losses and the spread of qubit-resonator couplings, which must be addressed to reach high-fidelity operations.

DOI: [10.1103/PRXQuantum.3.040322](https://doi.org/10.1103/PRXQuantum.3.040322)

I. INTRODUCTION

Quantum computers will enable efficient solutions to problems that are currently intractable for classical computers [1–4]. Among the many models of quantum computation is the gate-based quantum computer, which uses gates to act upon a register of qubits. An algorithm can be broken down into single-qubit operations and two-qubit entangling gates. However, as the leading quantum processors today are limited to 50–100 qubits and each qubit is sensitive to decoherence [often referred to as noisy intermediate-scale quantum (NISQ) devices [5]], running algorithms with a large circuit depth remains difficult. High-fidelity multiqubit gates are therefore central for reducing the circuit depth [6,7].

Superconducting circuits are a promising platform for quantum computation, due to advances in scaling up

microfabrication technology, individual qubit control and readout, and growing qubit coherence time [8,9]. However, the generation of high-fidelity multiqubit entanglement on cQED platforms, especially for three or more qubits, remains difficult, as multiqubit gates are limited by connectivity between qubits, noise in controls, and frequency crowding [8,10]. In particular, the connectivity of superconducting qubits is a design challenge, as it is difficult to place $O(n^2)$ qubits in an area that fits $O(n)$ qubits [7]. Processors with nearest-neighbor connectivity can only use cascaded pairwise interactions to generate multiqubit gates [11–13], which does not reduce the circuit depth. In contrast, tunable qubits coupled to a common bus resonator have the advantage of all-to-all coupling and can entangle by tuning into to near resonance with each other [14]. However, tunable qubits leave a larger footprint on already crowded processors, since each qubit requires an additional flux line, and they generally have shorter coherence times than fixed-frequency qubits, making it more difficult to scale.

To address these issues, we present the multiqubit sideband tone-assisted Rabi-driven (STAR) gate on a superconducting quantum processor with four Rabi-driven fixed-frequency qubits that are all-to-all connected

*Correspondence email address: marielu@berkeley.edu

Published by the American Physical Society under the terms of the [Creative Commons Attribution 4.0 International](https://creativecommons.org/licenses/by/4.0/) license. Further distribution of this work must maintain attribution to the author(s) and the published article's title, journal citation, and DOI.

through a bus resonator. We trade flux tunable qubits for Rabi dressing to harness the advantages of dynamical decoupling, reduce the footprint per qubit, and simplify fabrication restrictions. We demonstrate two-qubit entanglement with a maximum state fidelity of 95% (minimum 87%, average 91%), three-qubit entanglement with a 90.5% state fidelity, and four-qubit entanglement with a fidelity of 66%. In addition, we further characterize the two-qubit gate using quantum process tomography [15,16]. Moreover, we develop a model of the entangling gate as a blueprint for future scaling.

This gate is reminiscent of the trapped-ion-qubit Mølmer-Sørensen (MS) gate [17–19] with a few key differences that can be traced to the distinct energy scales in superconducting circuits and trapped-ion systems. As in the original Mølmer-Sørensen scheme, we use bichromatic sidebands to engineer the interaction between the qubits, as indicated by the red and blue arrows in Fig. 1(a). But while the original ion platform achieves all-to-all coupling through a shared phononic degree of freedom, we exchange this for a coplanar-waveguide resonator (CPW). Next, this difference in coupling and qubit platform causes an inversion between the qubit and coupling-mode energy scales when comparing the ion and transmon gates [Fig. 1(b)]. For ions, the high-frequency (gigahertz) spin degrees of freedom σ_i are coupled to the low-frequency (megahertz) vibrational mode \mathbf{a} of the ion chain. The sidebands, which are set at the sum and difference of the frequencies of these two modes, drive the spin degrees of freedom, resulting in resonant hopping terms such as $\sigma_i^\pm \mathbf{a}$. In the transmon case, the photonic mode is the highest frequency scale, at around 8 GHz, similar to the

qubit frequency. If we were to generate sidebands at the sum and difference frequencies of the resonator and qubit modes, we would have sidebands that are over 10 GHz apart. These sidebands, which must be sent into the shared CPW resonator, would largely be filtered out by the line width of the CPW resonator. Given that our resonators have kilohertz or megahertz intrinsic line width, the sidebands must be close in frequency to the shared resonator such that enough power can reach the qubits, requiring a much lower qubit energy than typical values.

A key technique used in this gate that both addresses this energy-scaling problem and supports its scalability is the addition of a Rabi drive on each qubit. We apply a drive to each participating qubit at its $|g\rangle \leftrightarrow |e\rangle$ transition frequency to enable a Rabi splitting and form new Rabi-dressed qubits with energy levels set by the amplitude of the Rabi drive, Ω , an experimentally tunable parameter [20]. Utilization of these dressed states allows us to reduce restrictions on qubit frequencies during fabrication and the need for tunable qubits. These features support scalability, as they reduce the number of lines needed to address each qubit and this simplifies the fabrication process. These advantages of Rabi-driven qubits have been further studied and proven to exhibit similar increased coherence properties due to dynamical decoupling in Refs. [21–27].

II. CIRCUIT-QED IMPLEMENTATION

The experimental implementation details are shown in Fig. 1. The four-qubit processor in Fig. 1(d) displays fixed-frequency transmons that have qubit frequencies $\omega_{\text{ge}}^{0,1,2,3}/2\pi = 5.24, 5.37, 5.69, \text{ and } 5.48$ GHz,

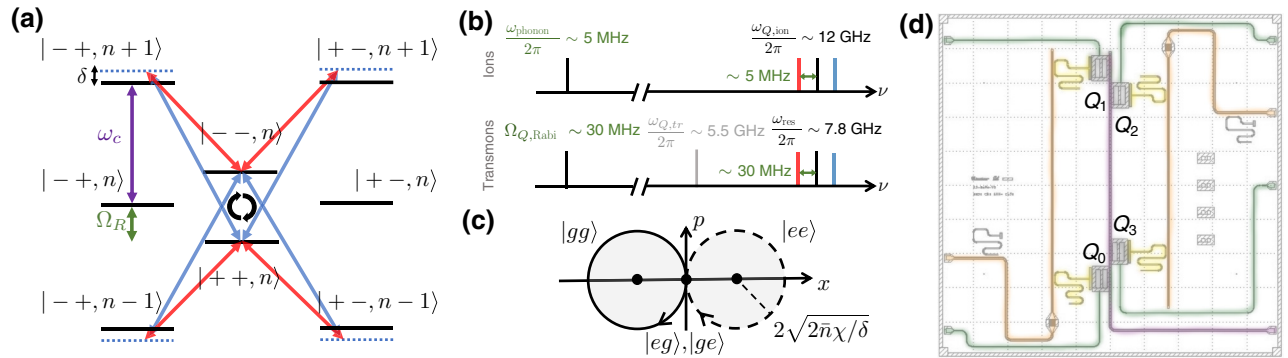


FIG. 1. (a) An experimental implementation on fixed-frequency transmons. The energy-level diagram for the Rabi-driven qubit states with n photons in the resonator and the sidebands at frequencies ω_r and ω_b . The red and blue sidebands drive two-photon transitions that generate a population swap between the $|--, n\rangle$ and $|++, n\rangle$ levels. (b) The different energy scales used in the gate implementation. The top diagram shows the relevant energies for ion qubits and the bottom diagram shows the implementation for Rabi-driven qubits. (c) Trajectories in the \mathbf{x} - \mathbf{p} plane of the resonator conditioned on the undriven qubit states. The black dots correspond to the displaced vacuums for the corresponding colored states (eigenvalues of α). During the course of the gate, the resonator makes a circle in phase space, entangling and subsequently disentangling with the coupled qubits at a rate $1/\delta$. (d) The chip design with qubit control lines in green, the shared resonator in purple ($\omega_c/2\pi = 7.82$ GHz), the readout resonators in yellow ($\omega_{\text{RO}}^k/2\pi = 6.4, 6.5, 6.8, \text{ and } 6.6$ GHz), and the Purcell filters in orange. The four transmon qubits are the gray rectangles just off of the shared resonator ($\omega_{\text{ge}}^k = 5.24, 5.37, 5.69, \text{ and } 5.48$ GHz).

anharmonicity $\alpha/2\pi = -240$ MHz, and dispersive shifts to the common bus mode $\chi_{0,1,2,3}/2\pi = 380, 410, 718,$ and 815 kHz. The resonator frequency is $\omega_c/2\pi = 7.82$ GHz and has a line width κ of 180 kHz. This value is dominated by the internal loss of the resonator, as the designed κ_{ext} is only 20 kHz. The qubit transitions relevant for the gate are the Rabi split states $|\pm\rangle = (|e\rangle \pm |g\rangle)/\sqrt{2}$ generated by applying drives at each qubit frequency, ω_{ge}^k . These are the states displayed in the two-qubit level diagram in Fig. 1(a), where n labels the photon occupation of the shared resonator. The red and blue sideband tones are applied to the resonator, with frequencies $\omega_r = \omega_c - \Omega_R + \delta$ and $\omega_b = \omega_c + \Omega_R + \delta$. Here, δ is the common detuning of the sideband tones. As indicated by the thick black arrows in Fig. 1(a), these sidebands drive two-photon transitions that result in population swaps between $|++, n\rangle$ and $|--, n\rangle$ if the qubits are prepared in either $|++, n\rangle$ or $|--, n\rangle$. We note that one may also initialize the qubits in $|+-, n\rangle$ and generate population swaps with $|+-, n\rangle$.

In the frame rotating at the qubit frequencies and at $\omega_c + \delta$ for an n -qubit gate, the dispersive Hamiltonian describing the system is given by [28]

$$\mathbf{H}_I = -\delta \mathbf{a}^\dagger \mathbf{a} + \sum_{k=1}^n (\Omega_R/2) \sigma_{x_k} - \chi_k \sigma_{z_k} \mathbf{a}^\dagger \mathbf{a} + \mathbf{H}_{\text{sb}}(t). \quad (1)$$

Here, \mathbf{a} is the annihilation operator of the resonator and σ_{l_k} , $l = x, y, z$, are the Pauli matrices of qubit k . The effect of the sideband term $\mathbf{H}_{\text{sb}}(t)$ acting on the resonator mode is to displace the field of the resonator such that $\mathbf{a} = d + \alpha(t)$, with $\alpha(t) = \sqrt{2\bar{n}} \cos(\Omega_R t + \varphi_\Delta)$, where \bar{n} is the mean resonator photon number due to the two sideband tones and φ_Δ is the phase difference of the two tones. After performing the displacement transformation and going into the qubit frame at the Rabi frequency (for details, see the Appendix), the Hamiltonian reduces to

$$\mathbf{H}_R = -\delta d^\dagger d - 2\sqrt{2\bar{n}} \chi \mathbf{J}_{zy}^{\varphi_\Delta} (d + d^\dagger) + \mathbf{H}_{\text{err}}, \quad (2)$$

where $\mathbf{J}_{\varphi_\Delta} = \cos(\varphi_\Delta) \mathbf{J}_z - \sin(\varphi_\Delta) \mathbf{J}_y$ and $\mathbf{J}_l = \sum_k \sigma_{l_k}/2$, $l = x, y, z$ are the generalized spin operators and $\mathbf{H}_{\text{err}} = \mathbf{A}_1 e^{i\Omega_R t} + \mathbf{A}_1 e^{2i\Omega_R t} + \text{h.c.}$ are spurious oscillating terms [26]. The effect of these terms can be neglected in the limit of large Rabi frequency, $\delta \sim \chi \sqrt{\bar{n}} < \chi \bar{n} \ll \Omega_R$. In this parameter regime, the Hamiltonian of Eq. (2) can be mapped to the Hamiltonian originally proposed by Mølmer and Sørensen in the context of trapped ions.

Here, we give a brief review of the working principle of the STAR gate. During the gate, the qubits entangle with the resonator field, resulting in a nontrivial operation on the qubits $U = e^{i\pi/2 \mathbf{J}_{\varphi_\Delta}^2}$. The origin of this nontrivial phase comes from the qubit-state-dependent paths that the resonator describes in phase space. To see this, one can cast the Hamiltonian of Eq. (2) in the form $\mathbf{H}_R = -\delta(d^\dagger -$

$\alpha^*)(d - \alpha) - \alpha^2$, with $\alpha = 2\chi \sqrt{2\bar{n}} \mathbf{J}_{\varphi_\Delta} / \delta$. The first term describes a harmonic oscillator of frequency δ centered on the term α , which contains the state dependent component $\mathbf{J}_{\varphi_\Delta}$, while the second term $\alpha^2 = 8\bar{n} \chi^2 \mathbf{J}_{\varphi_\Delta}^2 / \delta^2$ describes a qubit-qubit interaction term. Note that the two terms commute. Initializing the resonator field d in the vacuum, the field state remains in a coherent state and revolves around the qubit-dependent vacuum positions α , as depicted in Fig. 1(b). After one period of evolution $T = 2\pi/\delta$, the field state comes back to its initial position (the vacuum) and the qubits and the resonator disentangle. The qubits undergo a nontrivial evolution U generated by the last term $-\alpha^2$, with $U = \exp[i\pi(8\bar{n}\chi^2/\delta^2) \mathbf{J}_{\varphi_\Delta}^2]$. When $\delta = 2\sqrt{\bar{n}}\chi$, this implements the entangling gate $U = e^{i\pi/2 \mathbf{J}_{\varphi_\Delta}^2}$. With two qubits, U takes the simple form $U = e^{i\pi/2 \sigma_{zy,1}^{\varphi_\Delta} \sigma_{zy,2}^{\varphi_\Delta}}$ up to a global phase factor, where $\sigma_{zy,k}^{\varphi_\Delta} = \cos(\varphi_\Delta) \sigma_{z_k} - \sin(\varphi_\Delta) \sigma_{y_k}$. During the gate, the entanglement of the qubits with the resonator makes the gate fidelity sensitive to the resonator photon loss channel. In addition to $\chi \sqrt{\bar{n}} \ll \Omega_R$, we therefore require that the gate rate is much larger than κ , i.e., $\kappa \ll \chi \sqrt{\bar{n}}$.

To implement the gate, we begin by calibrating the parameters that are most important to our system: χ , \bar{n} , and κ . The combination of χ and \bar{n} sets the gate time and is used to calculate the sideband detuning δ_{sb} necessary for the gate [29]; whereas κ , the decay rate of photons from the shared resonator, sets a limit on the fidelity of the gate. We discuss this below when we analyze the sources of errors. The pulse sequence shown in Fig. 2(a) for the full gate shows a Rabi drive applied to each participating qubit. We rely on the single Rabi-driven qubit version of this pulse sequence to extract all three parameters. We point out that if one sets the state preparation and tomography pulses as $Y_\pi/2 = e^{-i\pi/4 \sigma_y}$, the gate pulse sequence is the classic spin-locking sequence, done on multiple qubits in parallel under the presence of sidebands [21]. We use this protocol as a form of chip and Hamiltonian characterization.

We provide an overview of our characterization procedure in Fig. 2. The level diagram for the single-qubit interaction with sidebands is shown in Fig. 2(b). We apply a state-preparation pulse to initialize the qubit(s) of interest, followed by a Rabi drive around the x axis to bring the qubits close to resonance with the sidebands. For instance, in Fig. 2(c), we sweep Ω_R with sideband frequencies fixed at $\nu_{\text{res}} + \Omega_R - \delta$ and $\nu_{\text{res}} - \Omega_R - \delta$ for $\Omega_R = 30$ MHz and detuning $\delta = 2.5$ MHz. The qubit is in resonance with the red (blue) sideband when $\Omega_R = 32.5$ (27.5) MHz. When Ω_R is far from resonance, the dynamics are set by a $T_{1,\rho}$ limited decay of the driven qubit [21], where $T_{1,\rho}$ is the dressed-frame analog of T_1 qubit relaxation. In contrast, when Ω_R is close to resonance, excitation swaps will occur in addition to the $T_{1,\rho}$ limited decay.

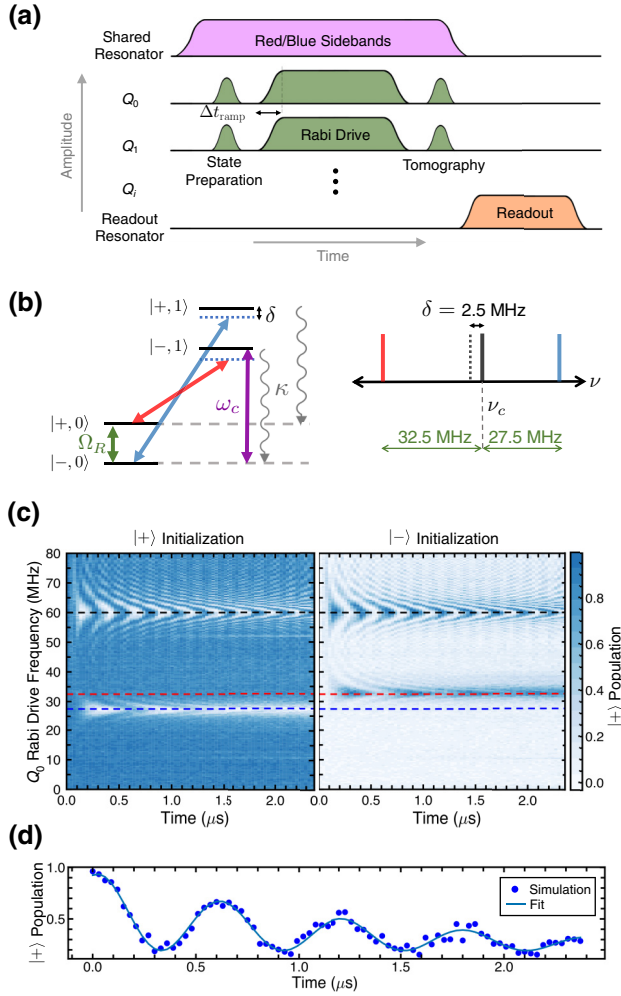


FIG. 2. The Hamiltonian characterization and gate calibration. (a) The pulse sequence for an n -qubit gate. The sequence for single-qubit calibrations and Hamiltonian spectroscopy is identical to the pulse sequence shown with $n = 1$. (b) The energy-level diagram for a Rabi-driven qubit and sidebands. κ is the dissipation out of the shared resonator. The choice of qubit initialization pulse determines whether κ will pin the qubit state in either $|+\rangle$ or $|-\rangle$. The sidebands are $2\Omega_R = 60$ MHz apart, with an overall 2.5-MHz detuning relative to the shared resonator frequency. (c) The spectroscopy of the Hamiltonian for a single qubit. Spectroscopy is performed by repeating the single-qubit pulse sequence in (a) with fixed sideband frequencies while sweeping the Rabi drive frequency, which changes the energy-level splittings shown in (b). With the sidebands set 60 MHz apart, the gate requires that the qubit Rabi drive be at 30 MHz, which is exactly in between the resonance features indicated by the red and blue dashed lines. (d) A cross section of (c) for $|+\rangle$ initialization at the blue dotted line. The continuous blue line is a fit of the data.

We use excitation swaps between the Rabi-driven qubit and resonator combined with a Stark-shift measurement to calibrate χ and \bar{n} . Where $\chi\bar{n} \gg \kappa$, these exchanges occur at a faster time scale than the loss out of the shared resonator. The red (blue) sideband drives population swaps between $|+, 0\rangle$ ($|-, 0\rangle$) and $|-, 1\rangle$ ($|+, 1\rangle$), shown in

Fig. 2(d), which is a cutaway of the full chevron in Fig. 2(c) for Q_0 . The rate of these oscillations is set by $\chi\sqrt{\bar{n}}$ and the observed exponential decay is set by κ , cooling the driven qubit to either $|+\rangle$ or $|-\rangle$ [29]. This contrasts with previous works studying the resonance features in the low χ/κ that show similar cooling effects without population swaps [29–31]. The frequency of the oscillations in Fig. 2(d) combined with the Stark shift of the qubit—which has a $\chi\bar{n}$ dependence—for different sideband powers allows us to calibrate χ and \bar{n} . We explain this in detail in the Appendix, along with other calibration measurements for the Rabi-drive power Ω_i and the sideband phase. We note that there is an additional resonance feature at 60 MHz, marked by the black dotted line in Fig. 2(c). This is generated by higher-order terms in the Hamiltonian due to the presence of the Rabi drive. In general, as discussed later, $\omega_b - \omega_r$ should be maximized so as to push this higher-frequency resonance away from the Rabi drive frequencies for the gate.

III. GATE CHARACTERIZATION

Next, we study the two-qubit population evolution over time to extract the gate time. To perform the gate, we implement the full pulse sequence in Fig. 2(a) on any desired subset of our qubits. We use Q_0 and Q_1 , two qubits with the most similar shared resonator dispersive couplings χ . The results for our choice of $|++\rangle$ initial state are summarized in Fig. 3. Maximum entanglement occurs when the $|+-\rangle$ and $|-\rangle$ populations reach a minimum and the $|++\rangle$ and $|--\rangle$ populations cross, as indicated by the vertical dashed line in Fig. 3(a). The gate time at that point is 310 ns, which refers to the length of the Rabi drive applied to each qubit. We prepare each of the four Bell states and perform state tomography at that gate time. The state fidelity [20], defined as

$$F = \sqrt{\sqrt{\rho}\sigma\sqrt{\rho}}, \quad (3)$$

ranges from 87% to 95%, with an average of 91%.

We further characterize our gate using quantum process tomography (QPT) [15,16], which is achieved by preparing 16 different input states and performing state tomography on each output state. A convenient set of input states that spans the two-qubit subspace is $\{|+\rangle, |-\rangle, |g\rangle, |i-\rangle\} \otimes \{|+\rangle, |-\rangle, |g\rangle, |i-\rangle\}$, where $|i-\rangle = (|+\rangle - i|-\rangle)/\sqrt{2}$. The measurement basis is chosen as $\sigma_m \otimes \sigma_n$, where $m, n = 0, x, y, z$ and $\sigma_0 = I$. Since we measure the qubits in the σ_z basis, we apply single-qubit tomographic pulses to measure the expectation values of $\sigma_i \otimes \sigma_j$. We present our results as a Pauli transfer matrix (PTM) in Fig. 3(b), which maps input Pauli state vectors to output Pauli state vectors. We then perform QPT on the two-qubit entangling interaction with a process fidelity of 81.6% between qubits 0 and 1. The

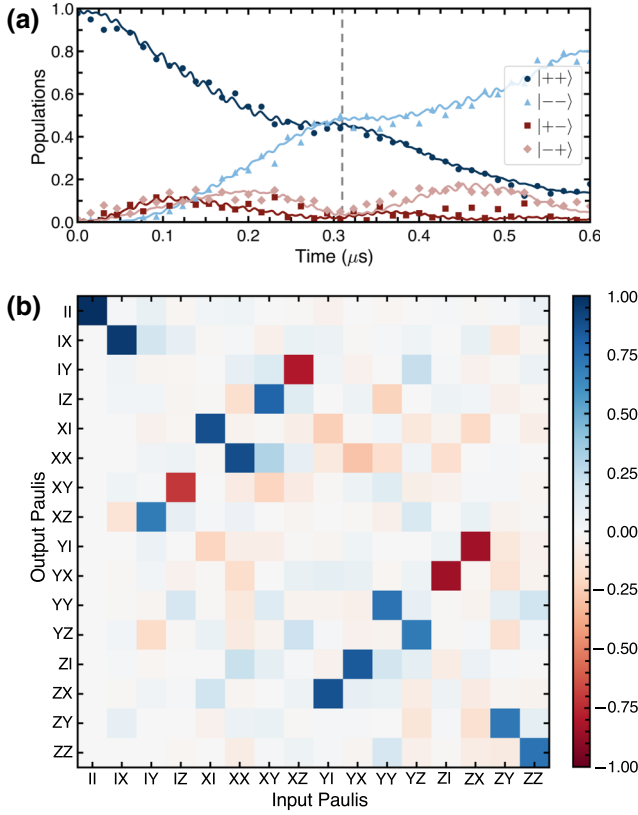


FIG. 3. Characterization of the two-qubit gate. (a) The gate evolution for two qubits: experimental data (points) together with simulations of Eq. (A7) (solid lines), with $\Omega_0/2\pi = 30.55$ MHz, $\Omega_1/2\pi = 29.92$ MHz, $\chi_0/2\pi = 380$ kHz, $\chi_1/2\pi = 410$ kHz, and $\kappa = 180$ kHz. (b) The Pauli transfer matrix (PTM) of the experimental data in the $|g/e\rangle$ basis, at $T_{\text{gate}} = 310$ ns, obtained by measuring 16 different initial states. The color bar represents the value of the PTM element. The process fidelity is 81.6%. The average fidelity to the target Bell state is given as 91.8%. The solid lines that fit each population are from simulations.

average state fidelity of all 16 initial states is 91.8%. We note that the qubit Rabi drive adds a global phase in the Rabi-driven qubit frame that we unwind using techniques described in the Appendix, resulting in the PTM shown. We also perform QPT on the identity operation with a process fidelity of 93.5% as a baseline check of state-preparation-and-measurement (SPAM) errors (see Fig. 10 in the Appendix).

The most important feature of the gate is its scalability, which we demonstrate by generating a three-qubit Greenberger-Horne-Zeilinger (GHZ) state on Q_0 , Q_1 , and Q_2 :

$$\Psi_{\text{GHZ}} = \frac{|ggg\rangle + |eee\rangle}{\sqrt{2}}. \quad (4)$$

We note here that for odd numbers of qubits, the Hamiltonian allows us to generate entanglement in either the

$|\pm\rangle$ basis or directly in the $|g/e\rangle$ basis, depending on the initial state and sideband phase. Given that the two bases have a direct mapping between them, we choose an initial-state and sideband-phase combination that directly entangles in the $|g/e\rangle$ basis for simplicity. We use a $Y_{\pi/2}$ pulse to prepare each qubit in the $|+\rangle$ state and then apply a σ_x Rabi drive to each qubit for 217 ns. Using individual qubit pulses to do state tomography, we find a state fidelity of 90.5%, similar to our two-qubit fidelities. The density matrix is shown in Fig. 4. We note that the three-qubit gate time is faster than the two-qubit gate time because the speed is proportional to the average χ_i and \sqrt{n} . We use the same sideband power for both gates, but the third added qubit has a much higher coupling than the first two qubits, thus raising the gate speed.

Finally, we attempt four-qubit GHZ state preparation and achieve a state fidelity of 66% in 200 ns. The density matrix is shown in Fig. 6 in the Appendix. Similar to before, the gate time is even shorter because the final added qubit has the highest χ of all qubits on our processor. The four-qubit fidelity is mainly limited by the large spread in χ and crosstalk between Q_2 and Q_3 . The Q_3 qubit frequency is very close to the $e \rightarrow f$ transition frequency for Q_2 . When both qubits are Rabi driven, as during the gate, we see a significant f state population for Q_2 . To mitigate this, we have to lower Ω_R for each qubit to 20 MHz, which further limits the fidelity. We discuss this in our error analysis.

IV. DISCUSSION AND ERRORS

We now turn to a study of the following sources of infidelity: SPAM errors, shared resonator decay (κ), spread in qubit-shared resonator couplings ($\Delta\chi$), δ calibration errors, pulse shaping, and the effects of a lower Rabi drive rate (Ω_R). Each error listed here is included in our simulations aside from SPAM errors.

The first major source of infidelity is due to SPAM errors. Process tomography of the identity process results in a process fidelity of 93.5%. Due to the nonzero κ of the shared resonator, we start the sideband pulse before the state-preparation pulse and perform all qubit operations, including the tomography pulses, in the presence of sidebands. However, the presence of sidebands decreases our qubit lifetimes and pulse quality (see the Appendix).

Assuming no SPAM errors, simulations based on Eq. (A7) (details can be found in the Appendix) suggest κ as one of the leading sources of error (a complete summary of the simulated accumulated error can be found in Table II). The effect of κ is shown in the decay of oscillations in Fig. 2(d). During the course of the gate, the resonator makes a circle in phase space [Fig. 1(c)] and changes its photon population by $\Delta n = 0.5$ as the qubits swap excitations with the resonator. This allows the qubits to each simultaneously entangle and then disentangle with

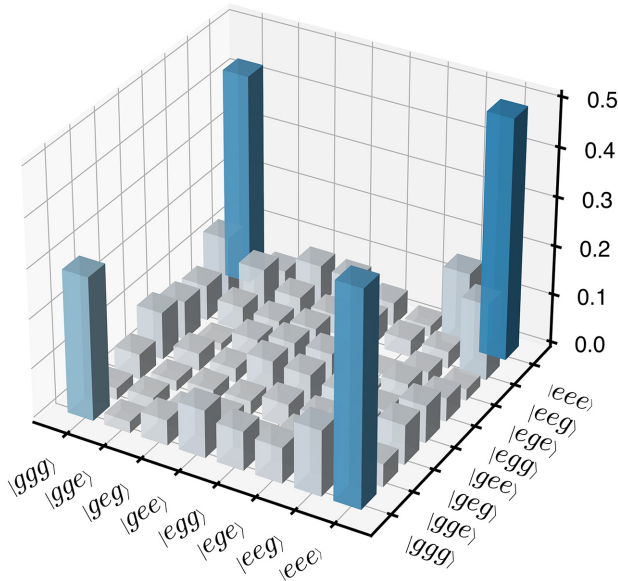


FIG. 4. Three-qubit entanglement: the density matrix for three qubits measured at gate time of 217 ns. The bars represent the amplitude of the density-matrix elements. We prepare the qubits in the $|+++ \rangle$ state and use the sideband phase calibrated to be 180° offset from the value used for the two-qubit interactions such that we entangle directly in the bare-qubit basis. Note here that the qubit states are labeled with $|g/e\rangle$ rather than $|\pm\rangle$. Entanglement in the \pm basis can be done by preparing in the $|i-\rangle$ state and using the same sideband phase as in the two-qubit measurements. We choose this for convenience.

the resonator, leaving the qubits entangled with one other. However, while the resonator is populated, photons may decay from the resonator. We design the external κ of the resonators to minimize the loss of photons during the gate. As such, the resonator loss is dominated by internal loss. We highlight this source of error first because we believe it is the most technically challenging to solve. While there have been demonstrations of high-quality-factor CPW resonators on chips without qubits [32], this has yet to be recreated on chips with qubits present and the additional fabrication steps may still lower the quality factor.

A second source of error that becomes more important with increasing qubit number is the spread of cross-Kerr couplings, $\Delta\chi$, between the qubits. We define $\Delta\chi = \max(\chi) - \min(\chi)/\text{avg}(\chi)$. Our simulations show that for a two-qubit gate, the contribution of $\Delta\chi$ to the infidelity is overshadowed by κ . The coupling strengths χ_i set the rate of the each segment of the two photon transition paths. If different qubits have different coupling strengths, then the various paths will have different rates of population transfer. Since the gate is the interference of all the various paths, the rates need to line up for to minimize the populations in the side states and achieve the highest fidelity possible. To verify this experimentally, we measure the two-qubit state fidelity between two qubits (Q_0 and Q_2)

that have the largest $\Delta\chi$ among the three qubits used for our multiqubit gate. We obtain a state fidelity of 93% for preparing $|++ \rangle + |-- \rangle/\sqrt{2}$, which is very similar to the maximum fidelities observed between Q_0 and Q_1 . However, for a three- and four-qubit gate, $\Delta\chi$ carries increasing weight in the infidelity. While the three-qubit gate uses the same qubits as in our two-qubit experiments, we see a drop in state fidelity as $\Delta\chi$ as a larger effect. This has an even greater effect for the four-qubit gate, as Q_2 and Q_3 have almost twice the coupling strength of Q_0 and Q_1 . We note that while the fidelity does strongly depend on $\Delta\chi$, the

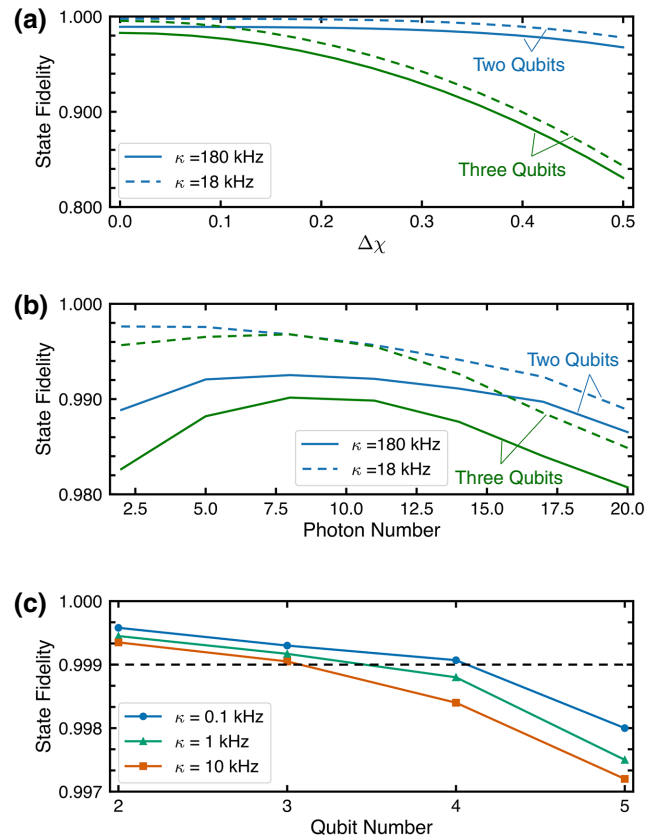


FIG. 5. Error analysis using simulations of Eq. (A7). (a) For a system composed of two (blue) or three (green) qubits, the fidelity of the gate is shown as a function of $\Delta\chi$. The two different styles of lines represent different κ values. We exclude qubit lifetimes in order to isolate the effect of the contribution of error due to $\Delta\chi$ and use the average of the $\chi_{\text{av}}/2\pi = 500$ kHz. (b) The state fidelity as a function of the mean photon number \bar{n} . A higher photon number raises the gate speed, which helps to mitigate the effect of lifetimes but also raises the contribution of counter-rotating terms that cause the fidelity to saturate at approximately ten photons. (c) The scaling of the entanglement fidelity as a function of N , the number of qubits, for the best possible achievable chip. The black dashed line marks the 0.999 fidelity threshold. We set $\Omega_R = 150$ MHz and $\chi_k = 1$ MHz while varying κ . All three figures take qubit lifetimes to the industry best values.

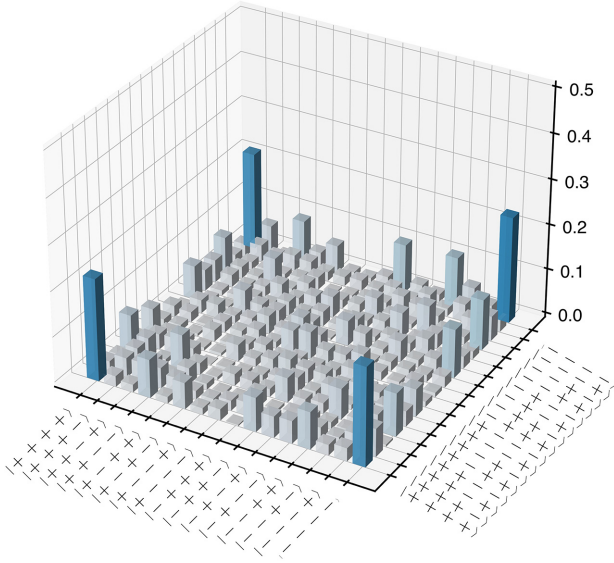


FIG. 6. The four-qubit density matrix. The bars represent the amplitude of the density-matrix elements.

couplings on this chip are anomalies due to design and fabrication errors and standard fabrication techniques should allow for $\Delta\chi$ values below 15%. We emphasize that for smaller values of $\Delta\chi$, κ will become the leading source of error that stands as a technical challenge.

To further describe the effects of κ and $\Delta\chi$, we again perform simulations with Eq. (A7) as a function of the parameters of interest. We summarize the effects of κ and $\Delta\chi$ in Fig. 5. In Figs. 5(a) and 5(b), we use resonator loss values that are similar to that on our sample and show fidelity dependence on key system parameters. We take qubit lifetimes to be infinite in order to isolate the effect of each parameter. Figure 5(a) shows the fidelity as a function of $\Delta\chi$, κ , and the number of qubits. Figure 5(b) shows expected fidelities as a function of the sideband power. While increasing \bar{n} raises fidelities at first because it decreases the gate time compared to loss rates, increased \bar{n} also widens the $2\Omega_R$ feature shown in Fig. 2(c), increasing the contribution of spurious counter-rotating terms in the Hamiltonian. Our simulations [Fig. 5(c)] suggest that

for leading fabrication techniques that produce resonators with quality factors over 5×10^6 and leading qubit coherence times [32,33], the gate can be implemented at or above the fault-tolerance threshold of 0.999 fidelity for up to four qubits. Furthermore, the STAR gate can be useful for running algorithms on NISQ processors for even higher numbers of qubits.

While κ and $\Delta\chi$ are the main error sources that we are able to characterize experimentally, there are a few additional contributions that are important to consider to optimize for the best attainable fidelities. We summarize the errors in Table I. First, we are currently not verifying how well the qubits disentangle from the shared resonator at the gate time. Ideally, a proper calibration of δ —obtained from our measurements of χ and \bar{n} —should ensure this but because we do not measure the state of the resonator, there is the possibility of an inaccurate calibration. As an example, from simulations, a miscalibration of δ by 10% on a two-qubit gate would add an additional 1.3% error. The second consideration is the finite ramp time used in the shape of the Rabi pulse. This ramp is necessary to keep the spectrum of the pulse narrow in frequency space. However, as the drive ramps up to the required Rabi frequency, it crosses a resonance with the sidebands. These are the same resonances used in the spin-locking measurements to calibrate our chip parameters in Fig. 2. These spurious interactions can be mitigated using pulse-optimization techniques [34,35].

The final source of error is the Rabi drive rate. As shown in the chevron plot in Fig. 2(c), there is a feature at frequency 2Ω marked by the black dotted line, at twice the Rabi drive frequency typically used for the gate at Ω_R . The frequency of the oscillations of the $2\Omega_R$ feature is at $2 \times 30 \text{ MHz} = 60 \text{ MHz}$ and the width of the oscillations is set by $\chi\bar{n}$. For higher sideband powers and lower Rabi drive frequencies, the oscillations generate counter-rotating terms in the Hamiltonian that interfere with gate dynamics. In our numerical simulations, the effects on the gate can be seen in Fig. 14 in the Appendix (comparing 30- and 60-MHz Rabi-drive gates). The fidelity of the two-qubit gate would benefit from increasing the Rabi drive to over 100 MHz or, equivalently, adding an

TABLE I. The error budget: the accumulated infidelity with each added term, descending, using parameter values that are currently found on our chip. The last item in the table includes an error in δ_{sb} is the only speculative error term, where we quote a 10% miscalibration to give a intuitive sense of scaling, but we are not currently measuring this value.

Error term	Infidelity (two qubits) (%)	Infidelity (three qubits) (%)	Infidelity (four qubits) (%)
$\Omega = 30 \text{ MHz}$	0.14	0.27	3.7 ($\Omega_R = 20 \text{ MHz}$)
$\kappa = 180 \text{ kHz}$	1.7	1.9	4.34
$\Delta\chi$	2.14	6.8	26.8
Qubit lifetimes	2.7	7.5	27.2
δ_{sb} miscalibration by 10%	4	11	30.5

TABLE II. The lifetimes of the four qubits without sidebands, all in microseconds. $T_{1,\rho}$ and $T_{2,\rho}$ are shown for a Rabi frequency of 30 MHz.

Qubit	T_1	$T_{2,\text{Ramsey}}$	$T_{2,\text{echo}}$	$T_{1,\rho}$	$T_{2,\rho}$
0	49.3 ± 14.1	13.2 ± 0.9	16.0 ± 0.9	50-60	28
1	57.0 ± 25.8	11.0 ± 4.7	13.9 ± 2.6	50-60	16
2	48.7 ± 5.9	15.1 ± 0.5	15.7 ± 0.3	60	45
3	23.8 ± 3.2	11.8 ± 3.4	12.9 ± 0.5	40	18

extra cancellation tone to offset the effects of the spurious feature.

This issue is exacerbated in our four-qubit demonstration, where we are required to lower the Rabi drive frequency to 20 MHz to reduce the crosstalk between Q_2 and Q_3 . However, such crosstalk should be mitigated by moving the processor to a three-dimensional (3D) integrated platform [36]. Currently, due to crosstalk, we must still limit the qubit frequencies such that neighboring qubit transition frequencies do not overlap. But a 3D integrated platform with reduced crosstalk should eliminate that requirement as well.

V. CONCLUSIONS AND OUTLOOK

In summary, we demonstrate a scalable maximally entangling gate on an all-to-all connected fixed-frequency transmon processor between two, three, and four qubits. The gate is generated through bichromatic microwaves and Rabi drives applied to each participating qubit. The Rabi drive provides the advantages of reducing limitations on qubit-qubit detunings during fabrication, dynamically decoupling from noise, and allowing us to entangle any subset of qubits on the chip. Finally, for the three-qubit gate, we are able to choose whether to entangle the qubits in the Rabi-dressed basis or the original qubit basis based on the sideband phase and preparation state, without the need for additional qubit pulses to map between bases. Looking forward, the gate is most limited by photon loss from the shared resonator for four and more qubits. The application of state-of-the-art fabrication techniques on a 3D integrated architecture will yield multipartite gates that exceed the 0.999 fidelity threshold for up to four qubits. At the same time, for gates with higher numbers of qubits, it is also worth exploring this scheme on parametrically coupled chips where we can perform the gate in a far-detuned regime, thus eliminating the κ loss factor.

ACKNOWLEDGMENTS

We would like to thank Lucas Buchmann, Felix Motzoi, Kyunghoon Lee, Ravi Naik, and Bradley Mitchell, for valuable discussions. This work was undertaken in part thanks to funding from the Natural Sciences and Engineering Research Council (NSERC), the Canada First

Research Excellence Fund, the Ministère de l'Économie et de l'Innovation du Québec, the U.S. Army Research Office under Grant No. W911NF-18-1-0411, the U.S. Department of Energy, Office of Science, National Quantum Information Science Research Centers and Quantum Systems Accelerator, and the L'Oréal USA For Women in Science Fellowship Program.

APPENDIX

1. Calibration of χ and \bar{n}

We use the combination of two measurements to calibrate the coupling strength of the qubit to sidebands: the spin-locking measurements with sidebands and qubit Stark-shift measurements as a function of the sideband power. Both measurements produce oscillations that we fit to extract the frequency. The resulting frequencies for the spin-locking and Stark-shift measurements exhibit different scalings with respect to the sideband power. In the spin-locking sequence, we repeat the measurement for several different red sideband powers, recording the resonant population swaps between $|+0\rangle$ and $|-1\rangle$. We fit the population evolution and extract the frequency of the oscillations, which has a $\chi\sqrt{\bar{n}}$ dependency and sets the strength of the couplings between the Floquet qubit and sidebands, as shown in Fig. 8. This $\chi\sqrt{\bar{n}}$ value sets the gate detuning and also the gate time. We also measure the Stark shift of the bare-qubit frequency as a function of the sideband strength using a Ramsey measurement, for which we expect a $\chi\bar{n}$ dependence. Combining these two relations, we obtain the χ values.

2. The Rabi drive

We sweep the amplitude of the qubit pulse for repeated Rabi-drive measurements. The population swaps between $|g\rangle$ and $|e\rangle$ are fit with a $\sin()$ function and the frequency is extracted. We then plot the frequencies as a function of the amplitude of the pulse, producing a linear dependence [Fig. 9(a)]. The linear fit is used to interpolate between the data points to select the amplitudes required for specific Rabi-drive frequencies.

3. Sideband-phase calibration

The phase difference of the sidebands and their relative phase compared to the qubit drive determines whether the Hamiltonian is an XX or a combination of XX and YY with respect to the $|\pm\rangle$ basis. Due to the fact that the Rabi pulse we use for the gate has a cosine edge, there is an extra accumulation of phase difference between the sidebands and the qubit drive, depending on the length of the cosine edge. We calibrate the sideband phase such that we implement the XX interaction. We can tune the gate angle $\varphi_{\Delta}^{\text{eff}} = \varphi_{\Delta}(t_r) - \Omega_R t_r = \varphi_{\Delta}(0) + \Omega_R t_r$ by adjusting the sideband

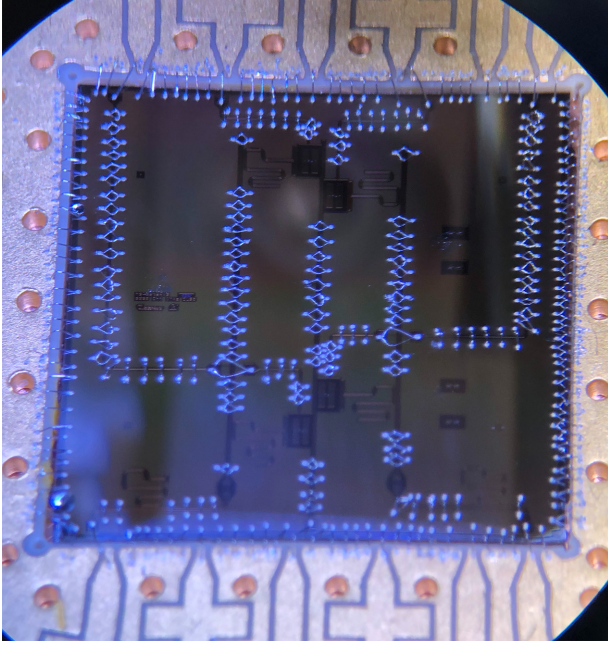


FIG. 7. The chip used for the experiment. Wire bonds to be used as air bridges were not yet available at time of fabrication.

phase difference $\varphi_{\Delta}(0)$. The angle is calibrated by initializing the qubits in $|00\rangle$, running the gate, and looking at the concurrence as a function of the sideband phase. The effective angle $\varphi_{\Delta}^{\text{eff}}$ is set to 0 when the concurrence is minimum. In Fig. 9(b), we show an example of this calibration.

4. Unwinding the Rabi drives of the gate

The gates applied on undriven transmon qubits commonly take place in the frame rotating at the mode frequencies. In the case of Rabi-driven qubits, the system undergoes the MS gate in the frame rotating at the Rabi frequencies. As the latter is not kept constant throughout the entire pulse sequence and as the tomography is done in the original undriven frame, we need to track and unwind the accumulated phase to characterize the gate.

The Rabi-drive pulse, of duration t_p , consists a square amplitude pulse, of duration t_{sq} during which the entangling operation is happening, sandwiched between two cosine-edge ramps, of duration t_r . The gate occurs during the square pulse and we have $t_p = t_{\text{sq}} + 2t_r$.

Neglecting decoherence, the propagator corresponding to the full Rabi-drive pulse can be expanded as $U_{t_p,0} = U_{\text{down}}U_{\text{gate}}U_{\text{up}}$, with $U_{\text{down}} = U_{t_{\text{sq}}+2t_r,t_{\text{sq}}+t_r}$, $U_{\text{gate}}(t_{\text{sq}}) = U_{t_{\text{sq}}+t_r,t_r}$, and $U_{\text{up}} = U_{t_r,0}$. Note that the populations in Fig. 3 are plotted as a function of t_{sq} .

As the ramp time t_r is much shorter than the inverse gate rate, the qubit-resonator coupling is (almost) resonant only during the square pulse. Consequently, U_{down} and U_{up} consists of local operations on each qubit around the x axis (accumulated phase), given by $U_{\text{up-down}} =$

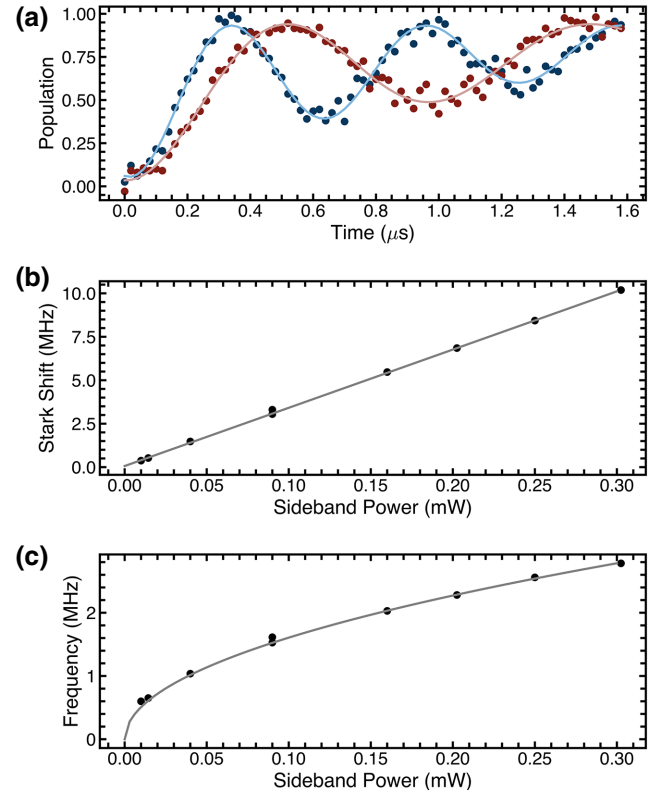


FIG. 8. The calibration of χ for qubit 3. (a) The results of the spin-locking measurement with sidebands on: oscillations between the $|+\rangle$ and $|-\rangle$ states observed for different powers of the sideband. We show two examples here at two different sideband strengths. (b) The Stark shift versus the power of the sidebands. (c) The frequency of the fitted oscillations from (a) versus the power of the sidebands.

$\exp(-i\Omega_R t_r \mathbf{J}_x / 2)$, where $\mathbf{J}_x = (\sigma_{x_1} + \sigma_{x_2})/2$. The factor $1/2$ in $U_{\text{up-down}}$ comes from the integral of the cosine-edge pulse. Here, we assume that the Rabi frequencies of the qubits are the same.

The propagator $U_{\text{gate}}(t_{\text{sq}})$ expands as $U_{\text{gate}}(t_{\text{sq}}) = U_R(t_{\text{sq}})U_{\text{gate}}^R(t_{\text{sq}})$, where $U_R(t_{\text{sq}}) = \exp(-i\Omega_R t_{\text{sq}} \mathbf{J}_x)$ represents the single-qubit phase accumulated during the gate and $U_{R,\text{gate}}(t_{\text{sq}}) = U_{t_{\text{sq}}+t_r,t_r}^R$ is the time-evolution operator generated by the Hamiltonian in Eq. (2). Since the two sideband tones are detuned from one another by $2\Omega_R$, the effective sideband phase difference φ_{Δ} of the gate depends on the time t_r at which the gate starts. More precisely, one can write $\varphi_{\Delta}(t_r) = \varphi_{\Delta}(0) + 2\Omega_R t_r$.

The global evolution operator can be cast in the convenient form $U_{t_p,0} = U_{\text{down}}U_R(t_{\text{sq}})U_{\text{up}}(U_{\text{up}}^\dagger U_{R,\text{gate}}^{\varphi_{\Delta}(t_r)}(t_{\text{sq}})U_{\text{up}})$. From the expression of $U_{\text{up-down}}$, we note that this operator applies a rotation on the qubits around the \mathbf{J}_x axis by an angle $\Omega_R t_r$ and its effect on $U_{R,\text{gate}}^{\varphi_{\Delta}(t_r)}(t_{\text{sq}})$ is merely to change the angle of the gate from $\varphi_{\Delta}(t_r)$ to $\varphi_{\Delta}^{\text{eff}} = \varphi_{\Delta}(t_r) - \Omega_R t_r$. Furthermore, the effective winding operator takes the form $U_{R,\text{eff}}(t_{\text{sq}}) = U_{\text{down}}U_R(t_{\text{sq}})U_{\text{up}} = \exp(-i\Omega_R(t_{\text{sq}} +$

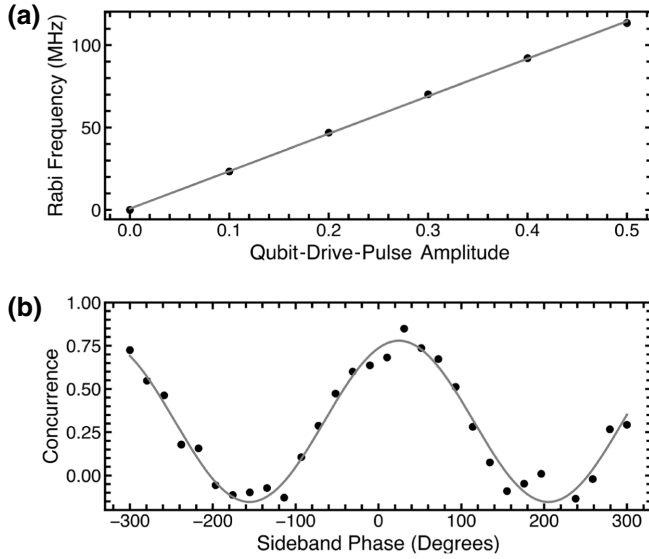


FIG. 9. Additional calibrations. (a) The fitted Rabi frequencies as a function of the amplitude of the qubit pulse used to perform the Rabi drive. (b) The sideband-phase calibration.

$t_r \mathbf{J}_x$), leading to $U_{t_p,0} = U_{R,\text{eff}}(t_{\text{sq}}) U_{R,\text{gate}}^{\phi_{\Delta}^{\text{eff}}}(t_{\text{sq}})$. By applying the unwinding operator $U_{R,\text{eff}}^{\dagger}(t_{\text{sq}})$ to the measured density matrix, we recover the density matrix resulting from the MS-gate evolution, $U_{R,\text{gate}}^{\phi_{\Delta}^{\text{eff}}}(t_{\text{sq}})$.

5. Rabi-driven qubits

State-of-the-art fixed-frequency qubits still have better lifetimes than flux-tunable frequency ones. Multiqubit gates, however, often require precise relations between the qubit frequencies, imposing strong requirements on fabrication. Here, we propose and implement the use of Rabi-driven Floquet qubits, with a tunable effective frequency, for quantum computation.

We start with the bare-frame Hamiltonian for a driven qubit:

$$H = -\frac{\omega_q}{2} \sigma_z + \Omega_R \cos(\omega_q t) \sigma_x. \quad (\text{A1})$$

Going into the frame rotating at the qubit frequency ω_z , or the dressed frame, the Hamiltonian of the Floquet qubit is $H_{\text{rot}} = \Omega_R \sigma_x$, with two eigenstates, $|+\rangle = (|g\rangle + |e\rangle)/\sqrt{2}$ and $|-\rangle = (|g\rangle - |e\rangle)/\sqrt{2}$, separated in energy by $2\Omega_R$.

a. Effect of sidebands on lifetimes

We perform a study of the qubit lifetimes with and without the presence of sidebands and find that the sidebands do not affect the T_1 lifetimes but do reduce T_2 by 1 μs on average for the sideband strengths used in the gate. To further characterize this extra loss, we perform a sweep of the sideband powers. The resulting Stark shift and dephasing are shown in Fig. 13.

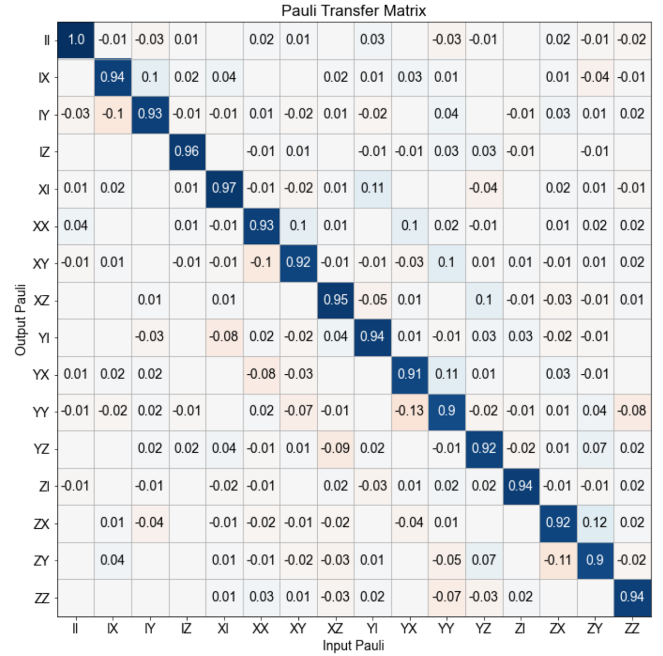


FIG. 10. The process tomography of the identity operation.

6. Quality of single-qubit pulses

We characterize the pulses via randomized benchmarking. The results vary for each qubit, ranging from $p = 0.985$ to 0.992 when sidebands are not on and from 0.98 to 0.985 when sidebands are on. A more complete characterization of the pulse and readout quality would be the PTM for the identity operation, shown in Fig. 10. The process fidelity for the identity operation is 93.5%.

7. Derivation of the MS Hamiltonian from bare-frame and driven qubits

Let us consider two transmon qubits coupled to a resonator through a Jaynes-Cummings Hamiltonian, two resonant Rabi drives applied to the transmons, and two sideband tones applied to the resonator. The Hamiltonian of the driven system can be written in the following form [38]:

$$\begin{aligned} \mathbf{H}(t)/\hbar = & \tilde{\omega}_c \mathbf{a}^\dagger \mathbf{a} + \sum_{k=1}^2 \tilde{\omega}_k \mathbf{b}_k^\dagger \mathbf{b}_k \\ & - \sum_{k=1}^2 E_J^k \left(\cos\left(\frac{\Phi_k}{\phi_0}\right) + \frac{1}{2} \frac{\Phi_k^2}{\phi_0^2} \right) \\ & + \sum_{k=1}^2 \Omega_{R_k}(t) i(\mathbf{b}_k^\dagger - \mathbf{b}_k) \\ & + i[\epsilon_r(t) + \epsilon_b(t)](\mathbf{a}^\dagger - \mathbf{a}), \end{aligned} \quad (\text{A2})$$

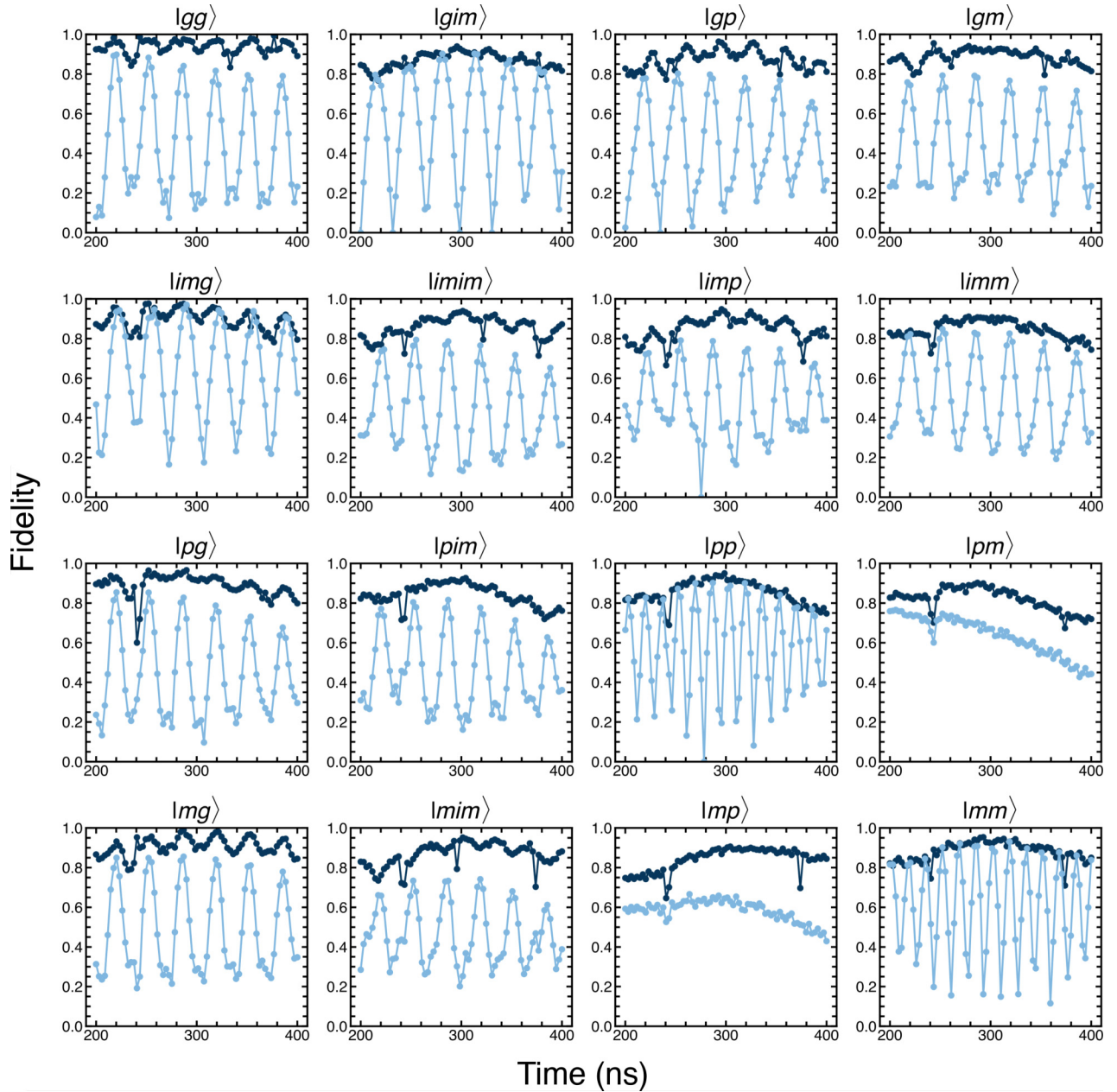


FIG. 11. Unwinding the global phase for process tomography: the fidelities to the target states for 16 different initial states labeled in the title of each subplot, used to construct the PTM of Fig. 3. The light blue points are the fidelities without removing the Rabi drive, exhibiting oscillations at 30 MHz for most initial states, at 60 MHz for $|+, +\rangle$, $|-, -\rangle$, and with no oscillations for $|+, -\rangle$, $|-, +\rangle$. The dark blue points are the processed data that have been unwound. The points at $t = 300$ ns give an average fidelity of 92%.

where

$$\Phi_k = \phi_k^a (\mathbf{a} + \mathbf{a}^\dagger) + \sum_{k'=1}^2 \phi_{k,k'}^b (\mathbf{b}_{k'} + \mathbf{b}_{k'}^\dagger),$$

in which we denote by \mathbf{a} (\mathbf{a}^\dagger) and \mathbf{b}_k (\mathbf{b}_k^\dagger) the annihilation (creation) operator of the resonator and qubit k , by

$\tilde{\omega}_c$ and $\tilde{\omega}_k$ the dressed frequencies of the resonator and qubit k , respectively, by E_J^k the Josephson energy of qubit k , and by $\phi_0 = \hbar/2e$ the superconducting flux quantum. The drives applied to the resonator (the transmons) also weakly drive the transmons (the resonators) through the hybridization. However, if the frequencies of the system are well separated, these terms can be neglected.

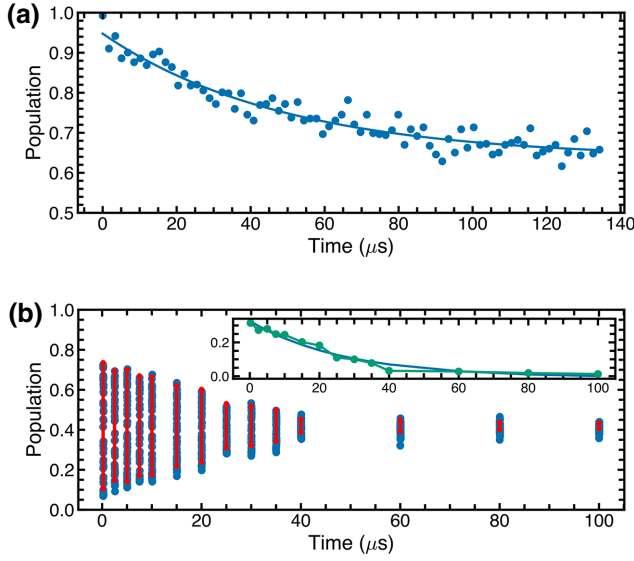


FIG. 12. Examples of $T_{1,\rho}$ and $T_{2,\rho}$ measurements. (a) A sample $T_{1,\rho}$ measurement obtained from performing a spin-locking pulse sequence. The lifetimes are extracted by fitting an exponential model. (b) An example of a $T_{2,\rho}$ measurement. We sample a Rabi measurement at different times and extract the maximum amplitudes (green points in the inset). We fit the amplitude of Rabi oscillations at different times. Here, $T_{2,\rho} = 27 \mu\text{s}$.

Noting that $\phi_k^a \ll \phi_{j,j}^b$, the dressed mode \mathbf{a} shares a much smaller part of the nonlinearity than the dressed modes \mathbf{b}_k . This is why we refer to the b modes as the qubit modes and the a modes as the cavity modes. In the transmon regime, the zero-point phase fluctuations of the modes are small and we can limit the expansion of the cosine to fourth order. Assuming that the frequencies of the system are well

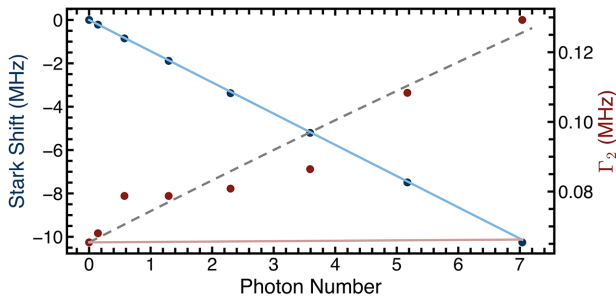


FIG. 13. Stark shift and dephasing with two sidebands. The blue points correspond to the Stark shift experienced by the qubit. The blue line indicates the linear fit. The red points correspond to the measurement-induced dephasing and the red line is the expected dephasing according to Ref. [37]. We see a large difference between the expected dephasing and the measured values. We believe that the presence of additional thermal photons could be responsible for this discrepancy and the dashed black line corresponds to the predicted dephasing with the added effect of thermal photons.

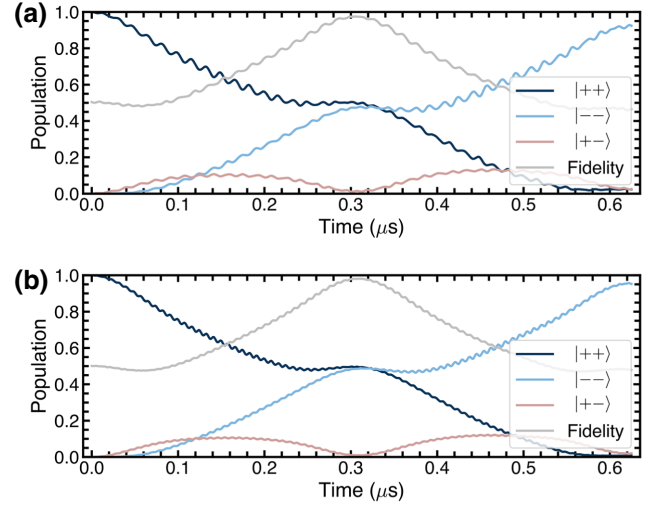


FIG. 14. The effect of higher-order terms due to the Rabi drive. We show the simulated populations as a function of time after initializing the qubits in $|--\rangle$ for couplings and Rabi drives similar to what is present on our processor. These simulations are obtained from simulating Eq. (A7). The evolution shows that the $|++\rangle$ and $|--\rangle$ populations meet at around 300 ns. Simultaneously, the $|+-\rangle$ and $|-+\rangle$ populations are at their lowest at 300 ns. This should be the time of maximum entanglement. In addition, we show a comparison of the population evolution between a gate performed using (a) 30-MHz Rabi drives and one using (b) 60-MHz Rabi drives.

separated and that $|\tilde{\omega}_k - \tilde{\omega}_j| \gg \Omega$, where Ω is the common Rabi frequency, the Hamiltonian simplifies to

$$\begin{aligned} \mathbf{H}(t)/\hbar = & \omega_c \mathbf{a}^\dagger \mathbf{a} + \sum_{k=1}^2 \omega_k \mathbf{b}_k^\dagger \mathbf{b}_k - K_k \mathbf{b}_k^{\dagger 2} \mathbf{b}_k^2 \\ & - \mathbf{a}^\dagger \mathbf{a} \left(\sum_{k=1}^2 \chi_k \mathbf{b}_k^\dagger \mathbf{b}_k \right) - \sum_{j \neq k} \chi_{j,k} \mathbf{b}_j^\dagger \mathbf{b}_j \mathbf{b}_k^\dagger \mathbf{b}_k \\ & + \sum_{k=1}^2 \Omega_{R_k}(t) i(\mathbf{b}_k^\dagger - \mathbf{b}_k) \\ & + i[\epsilon_r(t) + \epsilon_b(t)](\mathbf{a}^\dagger - \mathbf{a}), \end{aligned} \quad (\text{A3})$$

where ω_a and ω_k are the renormalized frequencies, χ_k , $\chi_{j,k}$, and K_k are, respectively, the cross-Kerr coefficient between the resonator and qubit k , the cross-Kerr coefficient between qubit j and qubit k , and the self-Kerr coefficient of qubit k . The Rabi drives and the sideband tones take the forms $\Omega_{R_k}(t) = \Omega_k \cos(\omega_k t)$ and $\epsilon_{r/b}(t) = \epsilon_r \cos[(\omega_c + \Omega_{r/b})t + \varphi_{r/b}]$, where $\Omega_{r/b}$ is the detuning of the tone from the resonator frequency.

We can write $\Omega_r = -\Omega_{\text{SB}} + \delta$, and $\Omega_b = \Omega_{\text{SB}} + \delta$, where δ is a small detuning compared to Ω_{SB} . We eliminate the drive term in the Hamiltonian by applying the

displacement on the cavity:

$$\begin{aligned} \mathbf{a} &= d + \alpha(t), \\ \alpha(t) &= \frac{\epsilon_r e^{-i\phi_r}}{2i} \left(\frac{e^{-i(\omega_a - \Omega_{\text{SB}} + \delta)t}}{-\Omega_{\text{SB}} + \delta} + \frac{e^{i(\omega_a - \Omega_{\text{SB}} + \delta)t}}{2\omega_a - \Omega_{\text{SB}} + \delta} \right) \\ &\quad + \frac{\epsilon_b e^{-i\phi_b}}{2i} \left(\frac{e^{-i(\omega_a + \Omega_{\text{SB}} + \delta)t}}{\Omega_{\text{SB}} + \delta} + \frac{e^{i(\omega_a + \Omega_{\text{SB}} + \delta)t}}{2\omega_a + \Omega_{\text{SB}} + \delta} \right). \end{aligned}$$

We choose ϵ_b and ϵ_r such that $|\epsilon_b|/(\Omega_{\text{SB}} + \delta) = |\epsilon_r|/(-\Omega_{\text{SB}} + \delta) = \sqrt{\bar{n}}$. As $|\epsilon_{r/b}| \ll 2\omega_a \pm \Omega_{\text{SB}} + \delta$, we can discard the terms that have $2\omega_a \pm \Omega_{\text{SB}} + \delta$ in the denominator. The amplitude of the classical field becomes simply $\alpha(t) = \sqrt{2\bar{n}} \cos(\Omega_{\text{SB}}t + \phi_\Delta) e^{-i[(\omega_c + \delta)t + \phi_\Sigma]}$, where $\phi_\Sigma = \phi_r + \phi_b + \pi/2$ and $\phi_\Delta = \phi_b - \phi_r/2$. We drop the phase factor $e^{-i\phi_\Sigma}$, as it can be eliminated by the transformation $\mathbf{a} \rightarrow \mathbf{a} e^{i\phi_\Sigma}$.

Moving to the frame rotating at the frequencies $\omega_a + \delta$ and ω_k , and discarding the counter-rotating terms, the Hamiltonian becomes

$$\begin{aligned} \mathbf{H}(t)/\hbar &= -\delta d^\dagger d - \sum_{k=1}^2 K_k \mathbf{b}_k^{\dagger 2} \mathbf{b}_k^2 \\ &\quad - (d^\dagger d + \sqrt{2\bar{n}} \cos(\Omega_{\text{SB}}t + \phi_\Delta)(d^\dagger + d) \\ &\quad + 2\bar{n} \cos^2(\Omega_{\text{SB}}t + \phi_\Delta)) \left(\sum_{k=1}^2 \chi_k \mathbf{b}_k^\dagger \mathbf{b}_k \right) \\ &\quad - \sum_{j \neq k}^2 \chi_{j,k} \mathbf{b}_j^\dagger \mathbf{b}_j \mathbf{b}_k^\dagger \mathbf{b}_k \\ &\quad + \sum_{k=1}^2 \Omega_k \cos(\omega_k t) i(\mathbf{b}_k^\dagger e^{i\omega_k t} - \mathbf{b}_k e^{-i\omega_k t}). \quad (\text{A4}) \end{aligned}$$

From this more complete form of the Hamiltonian, we note two possible limitations to the performance of the gate: first, the cross-Kerr or ZZ interaction, which becomes a resonant XX interaction when the Rabi drives are on; and, second, another limitation due to the finite ratio of the Rabi frequency over the anharmonicity of the transmons, Ω_k/K_k .

Assuming that the anharmonicity of the transmons remains larger than the Rabi frequency, i.e., $K_k/\Omega_k \gg 1$, we can make a two-level approximation and project the above Hamiltonian on the ground and excited states of the transmons. In addition, we neglect the cross-Kerr between the qubits mediated by the resonator and perform a rotating-wave approximation on the Rabi-drive terms,

leading to

$$\begin{aligned} \mathbf{H}(t)/\hbar &= -\delta d^\dagger d + \sum_{k=1}^2 \frac{\Omega_k}{2} \sigma_{x_k} \\ &\quad - (d^\dagger d + \sqrt{2\bar{n}} \cos(\Omega_{\text{SB}}t + \phi_\Delta)(d^\dagger + d) \\ &\quad + 2\bar{n} \cos^2(\Omega_{\text{SB}}t + \phi_\Delta)) \left(\sum_{k=1}^2 \tilde{\chi}_k \sigma_{z_k} \right), \quad (\text{A5}) \end{aligned}$$

where $\tilde{\chi}_k = \chi_k/2$. In the following and in Sec. II of the main text, we take the definition $\chi_k := \tilde{\chi}_k$. Setting $\Omega_k = \Omega_{\text{SB}}$ and $\chi_k = \chi$ for all k and going into the frame rotating at the Rabi-drive frequency, the Hamiltonian becomes that of Eq. (2),

$$\mathbf{H}_R = -\delta d^\dagger d - 2\sqrt{2\bar{n}} \chi \mathbf{J}_{z\Delta}^\varphi (d + d^\dagger) + \mathbf{H}_{\text{err}}(t), \quad (\text{A6})$$

where $\mathbf{J}_{\varphi_\Delta} = \cos(\varphi_\Delta) \mathbf{J}_z - \sin(\varphi_\Delta) \mathbf{J}_y$ and $\mathbf{J}_l = \sum_k \sigma_{l_k}/2$, $l = x, y, z$, are the generalized spin operators and $\mathbf{H}_{\text{err}} = \mathbf{A}_1 e^{i\Omega_{\text{SB}}t} + \mathbf{A}_1 e^{2i\Omega_{\text{SB}}t} + \mathbf{h.c.}$ represents spurious oscillating terms [26]. $\mathbf{H}_{\text{err}}(t)$ can be neglected as long as we satisfy $\|\mathbf{B}_{1,2}\| \ll \Omega_R$. The dominant term in $\mathbf{H}_{\text{err}}(t)$ comes from the term in the third line of Eq. (A5) and scales as $\chi \bar{n} e^{i\Omega t}$. This leads to a renormalization of the Rabi frequency that is taken into account in the simulations. This term is responsible for the fidelity saturation in Fig. 5(b). When the Rabi frequency is set to $\Omega_R = 2\Omega_{\text{SB}}$, this term becomes resonant and leads to the large oscillation of $\langle \sigma_X \rangle$ seen at $\Omega_R = 60$ MHz in Fig. 2(c).

8. Master equation

All simulations are obtained using the following master equation:

$$\begin{aligned} \frac{d\rho}{dt} &= -\frac{i}{\hbar} [\mathbf{H}(t), \rho] \\ &\quad + \sum_k \mathcal{D}[\sqrt{1/2 T_{1,\rho,k}} \sigma_{z_k}](\rho) \\ &\quad + \sum_k \mathcal{D}[\sqrt{1/2 T_{2,\rho,k}} \sigma_{z_x}](\rho) \\ &\quad + \mathcal{D}[\sqrt{\kappa} \mathbf{a}](\rho), \quad (\text{A7}) \end{aligned}$$

where $\mathcal{D}[\mathbf{M}](\rho) = \mathbf{M}\rho\mathbf{M}^\dagger - (\mathbf{M}^\dagger\mathbf{M}\rho + \rho\mathbf{M}^\dagger\mathbf{M})/2$. Here, $T_{1,\rho,k}$ and $T_{2,\rho,k}$ are the spin-locking times of qubit k and we use the Hamiltonian of Eq. (A5).

- [1] J. M. Chow, J. M. Gambetta, A. D. Córcoles, S. T. Merkel, J. A. Smolin, C. Rigetti, S. Poletto, G. A. Keefe, M. B. Rothwell, and J. R. Rozen, *et al.*, Universal Quantum Gate

- Set Approaching Fault-Tolerant Thresholds with Superconducting Qubits, *Phys. Rev. Lett.* **109**, 060501 (2012).
- [2] L. K. Grover, Quantum Mechanics Helps in Searching for a Needle in a Haystack, *Phys. Rev. Lett.* **79**, 325 (1997).
- [3] N. Brunner, D. Cavalcanti, S. Pironio, V. Scarani, and S. Wehner, Bell nonlocality, *Rev. Mod. Phys.* **86**, 419 (2014).
- [4] L. García-Álvarez, U. Las Heras, A. Mezzacapo, M. Sanz, E. Solano, and L. Lamata, Quantum chemistry and charge transport in biomolecules with superconducting circuits, *Sci. Rep.* **6**, 27836 (2016).
- [5] J. Preskill, Quantum computing in the NISQ era and beyond, *Quantum* **2**, 79 (2018).
- [6] K.-A. Brickman, P. C. Haljan, P. J. Lee, M. Acton, L. Deslauriers, and C. Monroe, Implementation of Grover's quantum search algorithm in a scalable system, *Phys. Rev. A* **72**, 050306 (2005).
- [7] D. Maslov and Y. Nam, Use of global interactions in efficient quantum circuit constructions, *New J. Phys.* **20**, 033018 (2018).
- [8] M. Kjaergaard, M. E. Schwartz, J. Braumüller, P. Krantz, J. I.-J. Wang, S. Gustavsson, and W. D. Oliver, Superconducting qubits: Current state of play, *Annu. Rev. Condens. Matter Phys.* **11**, 369 (2020).
- [9] A. Nersisyan, S. Poletto, N. Alidoust, R. Manenti, R. Renzas, C.-V. Bui, K. Vu, T. Whyland, Y. Mohan, E. A. Sete, S. Stanwyck, A. Bestwick, and M. Reagor, 2019 *IEEE International Electron Devices Meeting (IEDM)*, 31.1.1 (2019).
- [10] P. Krantz, M. Kjaergaard, F. Yan, T. P. Orlando, S. Gustavsson, and W. D. Oliver, A quantum engineer's guide to superconducting qubits, *Appl. Phys. Rev.* **6**, 021318 (2019).
- [11] G. J. Mooney, C. D. Hill, and L. C. Hollenberg, Entanglement in a 20-qubit superconducting quantum computer, *Sci. Rep.* **9**, 1 (2019).
- [12] M. Gong, *et al.*, Genuine 12-Qubit Entanglement on a Superconducting Quantum Processor, *Phys. Rev. Lett.* **122**, 110501 (2019).
- [13] K. X. Wei, I. Lauer, S. Srinivasan, N. Sundaresan, D. T. McClure, D. Toyli, D. C. McKay, J. M. Gambetta, and S. Sheldon, Verifying multipartite entangled Greenberger-Horne-Zeilinger states via multiple quantum coherences, *Phys. Rev. A* **101**, 032343 (2020).
- [14] C. Song, K. Xu, W. Liu, C.-p. Yang, S.-B. Zheng, H. Deng, Q. Xie, K. Huang, Q. Guo, L. Zhang, P. Zhang, D. Xu, D. Zheng, X. Zhu, H. Wang, Y.-A. Chen, C.-Y. Lu, S. Han, and J.-W. Pan, 10-Qubit Entanglement and Parallel Logic Operations with a Superconducting Circuit, *Phys. Rev. Lett.* **119**, 180511 (2017).
- [15] I. L. Chuang and M. A. Nielsen, Prescription for experimental determination of the dynamics of a quantum black box, *J. Mod. Opt.* **44**, 2455 (1997).
- [16] J. F. Poyatos, J. I. Cirac, and P. Zoller, Complete Characterization of a Quantum Process: The Two-Bit Quantum Gate, *Phys. Rev. Lett.* **78**, 390 (1997).
- [17] A. Sørensen and K. Mølmer, Quantum Computation with Ions in Thermal Motion, *Phys. Rev. Lett.* **82**, 1971 (1999).
- [18] A. Sørensen and K. Mølmer, Entanglement and quantum computation with ions in thermal motion, *Phys. Rev. A* **62**, 022311 (2000).
- [19] K. Mølmer and A. Sørensen, Multiparticle Entanglement of Hot Trapped Ions, *Phys. Rev. Lett.* **82**, 1835 (1999).
- [20] M. Nielsen and I. Chuang, *Quantum Computation and Quantum Information* (Cambridge University Press, Cambridge, UK, 2010).
- [21] F. Yan, S. Gustavsson, J. Bylander, X. Jin, F. Yoshihara, D. G. Cory, Y. Nakamura, T. P. Orlando, and W. D. Oliver, Rotating-frame relaxation as a noise spectrum analyser of a superconducting qubit undergoing driven evolution, *Nat. Commun.* **4**, 2337 (2013).
- [22] F. Yan, D. Campbell, P. Krantz, M. Kjaergaard, D. Kim, J. L. Yoder, D. Hover, A. Sears, A. J. Kerman, and T. P. Orlando, *et al.*, Distinguishing Coherent and Thermal Photon Noise in a Circuit Quantum Electrodynamical System, *Phys. Rev. Lett.* **120**, 260504 (2018).
- [23] Y. Sung, A. Vepsäläinen, J. Braumüller, F. Yan, J. I.-J. Wang, M. Kjaergaard, R. Winik, P. Krantz, A. Bengtsson, and A. J. Melville, *et al.*, Multi-level quantum noise spectroscopy, *Nat. Commun.* **12**, 967 (2021).
- [24] U. von Lüpke, F. Beaudoin, L. M. Norris, Y. Sung, R. Winik, J. Y. Qiu, M. Kjaergaard, D. Kim, J. Yoder, and S. Gustavsson, *et al.*, Two-Qubit Spectroscopy of Spatiotemporally Correlated Quantum Noise in Superconducting Qubits, *PRX Quantum* **1**, 010305 (2020).
- [25] U. Vool, S. Shankar, S. O. Mundhada, N. Ofek, A. Narla, K. Sliwa, E. Zaly-Geller, Y. Liu, L. Frunzio, R. J. Schoelkopf, S. M. Girvin, and M. H. Devoret, Continuous Quantum Nondemolition Measurement of the Transverse Component of a Qubit, *Phys. Rev. Lett.* **117**, 133601 (2016).
- [26] A. Eddins, S. Schreppler, D. M. Toyli, L. S. Martin, S. Hacohe-Gourgy, L. C. G. Govia, H. Ribeiro, A. A. Clerk, and I. Siddiqi, Stroboscopic Qubit Measurement with Squeezed Illumination, *Phys. Rev. Lett.* **120**, 040505 (2018).
- [27] L. Viola and S. Lloyd, Dynamical suppression of decoherence in two-state quantum systems, *Phys. Rev. A* **58**, 2733 (1998).
- [28] A. Blais, R.-S. Huang, A. Wallraff, S. M. Girvin, and R. J. Schoelkopf, Cavity quantum electrodynamics for superconducting electrical circuits: An architecture for quantum computation, *Phys. Rev. A* **69**, 062320 (2004).
- [29] K. W. Murch, U. Vool, D. Zhou, S. J. Weber, S. M. Girvin, and I. Siddiqi, Cavity-Assisted Quantum Bath Engineering, *Phys. Rev. Lett.* **109**, 183602 (2012).
- [30] C. Aron, M. Kulkarni, and H. E. Türeci, Steady-state entanglement of spatially separated qubits via quantum bath engineering, *Phys. Rev. A* **90**, 062305 (2014).
- [31] M. E. Kimchi-Schwartz, L. Martin, E. Flurin, C. Aron, M. Kulkarni, H. E. Türeci, and I. Siddiqi, Stabilizing Entanglement via Symmetry-Selective Bath Engineering in Superconducting Qubits, *Phys. Rev. Lett.* **116**, 240503 (2016).
- [32] M. V. P. Altoé, A. Banerjee, C. Berk, A. Hajr, A. Schwartzberg, C. Song, M. A. Ghadeer, S. Aloni, M. J. Elowson, J. M. Kreikebaum, E. K. Wong, S. Griffin, S. Rao, A. Weber-Bargioni, A. M. Minor, D. I. Santiago, S. Cabrini, I. Siddiqi, and D. F. Ogletree, Localization and reduction

- of superconducting quantum coherent circuit losses (2020), [ArXiv:2012.07604](https://arxiv.org/abs/2012.07604).
- [33] A. P. M. Place, L. V. H. Rodgers, P. Mundada, B. M. Smitham, M. Fitzpatrick, Z. Leng, A. Premkumar, J. Bryon, A. Vrajitoarea, S. Sussman, G. Cheng, T. Madhavan, H. K. Babla, X. H. Le, Y. Gang, B. Jäck, A. Gyenis, N. Yao, R. J. Cava, N. P. de Leon, and A. A. Houck, New material platform for superconducting transmon qubits with coherence times exceeding 0.3 milliseconds, *Nat. Commun.* **12**, 1779 (2021).
- [34] M. Werninghaus, D. J. Egger, F. Roy, S. Machnes, F. K. Wilhelm, and S. Filipp, Leakage reduction in fast superconducting qubit gates via optimal control, *npj Quantum Inf.* **7**, 14 (2021).
- [35] D. Dong, C. Wu, C. Chen, B. Qi, I. R. Petersen, and F. Nori, Learning robust pulses for generating universal quantum gates, *Sci. Rep.* **6**, 36090 (2016).
- [36] C. R. Conner, A. Bienfait, H.-S. Chang, M.-H. Chou, E. Dumur, J. Grebel, G. A. Peairs, R. G. Povey, H. Yan, Y. P. Zhong, A. N. Cleland, Superconducting qubits in a flip-chip architecture, *Appl. Phys. Lett.* **118**, 232602 (2021).
- [37] J. Gambetta, A. Blais, D. I. Schuster, A. Wallraff, L. Frunzio, J. Majer, M. H. Devoret, S. M. Girvin, and R. J. Schoelkopf, Qubit-photon interactions in a cavity: Measurement-induced dephasing and number splitting, *Phys. Rev. A* **74**, 042318 (2006).
- [38] S. E. Nigg, H. Paik, B. Vlastakis, G. Kirchmair, S. Shankar, L. Frunzio, M. H. Devoret, R. J. Schoelkopf, and S. M. Girvin, Black-Box Superconducting Circuit Quantization, *Phys. Rev. Lett.* **108**, 240502 (2012).

Correction: An incorrect version of the abstract was inserted during the proof production cycle and has been set right.